TU Delft

Delft University of Technology

Numerical analysis of vortex dynamics in hyperbolic funnels using computational fluid dynamics

Donepudi, T.; van de Griend, Maarten ; Agostinho, Luewton L.F.; Kroon, Esther J. de; Klymenko, Roman; Pecnik, Rene; Woisetschläger , Jakob; Fuchs, Elmar C

DOI
10.1063/5.0222216

Publication date
2024

Document Version
Final published version

Published in
Physics of Fluids

Citation (APA)
Donepudi, T., van de Griend, M., Agostinho, L. L. F., Kroon, E. J. D., Klymenko, R., Pecnik, R., Woisetschläger , J., & Fuchs, E. C. (2024). Numerical analysis of vortex dynamics in hyperbolic funnels using computational fluid dynamics. *Physics of Fluids*, *36*(9), Article 095171. https://doi.org/10.1063/5.0222216

Important note
To cite this publication, please use the final published version (if applicable).
Please check the document version above.

Copyright
Other than for strictly personal use, it is not permitted to download, forward or distribute the text or part of it, without the consent of the author(s) and/or copyright holder(s), unless the work is under an open content license such as Creative Commons.

Takedown policy
Please contact us and provide details if you believe this document breaches copyrights.
We will remove access to the work immediately and investigate your claim.

This work is downloaded from Delft University of Technology.
For technical reasons the number of authors shown on this cover page is limited to a maximum of 10.

Physics of Fluids

RESEARCH ARTICLE | SEPTEMBER 26 2024

Numerical analysis of vortex dynamics in hyperbolic funnels using computational fluid dynamics

Teja Donepudi ; Maarten van de Griend ; Luewton L. F. Agostinho ; Esther J. de Kroon; Roman Klymenko ; Rene Pecnik ; Jakob Woisetschläger ; Elmar C. Fuchs

Check for updates

Physics of Fluids 36, 095171 (2024)
https://doi.org/10.1063/5.0222216

View Online
Export Citation

Articles You May Be Interested In

Cavitation bubble dynamics in a funnel-shaped tube
Physics of Fluids (September 2022)

Mechanism of tornado funnel formation
Phys. Fluids (December 1976)

Directed drift and fluid pumping of nanoswimmers by periodic rectification-diffusion
J. Chem. Phys. (January 2017)

30 September 2024 13:54:38

AIP Publishing

Physics of Fluids
Special Topic:
Kitchen Flows 2024
Guest Editors: Gerald G. Fuller, Maciej Lisicki, Arnold J.T.M. Mathijssen, Endre Joachim Mossige, Rossana Pesquino, Vivek Nagendra Prakash, Laurence Ramos
Submit Today!
AIP Publishing

Physics of Fluids ARTICLE pubs.aip.org/aip/pof

Numerical analysis of vortex dynamics in hyperbolic funnels using computational fluid dynamics

Cite as: Phys. Fluids **36**, 095171 (2024); doi: 10.1063/5.0222216
Submitted: 6 June 2024 · Accepted: 27 August 2024 ·
Published Online: 26 September 2024

View Online Export Citation CrossMark

Teja Donepudi,[1] Maarten van de Griend,[2] Luewton L. F. Agostinho,[3,4] Esther J. de Kroon,[3] Roman Klymenko,[4] Rene Pecnik,[1] Jakob Woisetschläger,[5] and Elmar C. Fuchs[4,6,a)]

AFFILIATIONS

[1]Process and Energy Laboratory, Delft University of Technology, Leeghwaterstraat 39, 2628 CB Delft, The Netherlands
[2]Centre of Expertise Water Technology, Leeuwarden, The Netherlands
[3]Water Technology Research Group, NHL Stenden University of Applied Sciences, Rengerslaan 8-10, 8917 DD Leeuwarden, The Netherlands
[4]Wetsus, European Center of Excellence for Sustainable Water Technology, 8911 MA Leeuwarden, The Netherlands
[5]Working Group Metrology-Laser Optical Metrology, Institute for Thermal Turbomachinery and Machine Dynamics, Graz University of Technology, Inffeldgasse 25A, 8010 Graz, Austria
[6]Optical Sciences Group, Faculty of Science and Technology (TNW), University of Twente, Drienerlolaan 5, 7522 NB Enschede, The Netherlands

[a)]**Author to whom the correspondence should be addressed:** elmar.fuchs@wetsus.nl

ABSTRACT

Experimental investigations into the characterization of vortices in hyperbolic funnels have shown efficient aeration properties. Certain regimes of vortices have been observed to exhibit high gas dissolution rates. This phenomenon has prompted inquiries into the underlying physical mechanisms at both micro and macroscopic scales. The present study employs computational fluid dynamics to numerically analyze the flow field organization inside these vortices, aiming to elucidate the observed high gas transfer rates. Transient simulations are performed on a three-dimensional radially structured hexahedral mesh, utilizing a multiphase Euler–Euler approach-based volume of fluid method for modeling, along with shear stress transport turbulence modeling based on $k-\omega$ equations with curvature correction. The evaluation of the two vortex regimes was conducted in terms of hydraulic retention time, water volume in the reactor, air–water interfacial area, and bulk mixing. Instabilities resembling Taylor vortices observed in Taylor–Couette flow systems emerge in the secondary flow field of these vortical structures, facilitating turbulent mixing. A qualitative analysis of the strength of these instabilities in terms of average vorticity per unit mass of water explains the high gas transfer efficiency. Despite high gas transfer rates, water exiting the funnel remains undersaturated under given operating conditions due to the short hydraulic retention time.

© 2024 Author(s). All article content, except where otherwise noted, is licensed under a Creative Commons Attribution (CC BY) license (https://creativecommons.org/licenses/by/4.0/). https://doi.org/10.1063/5.0222216

I. INTRODUCTION

Vortices and spirals are a captivating natural phenomenon. They occur in many different forms and scales, from galaxies to the crystallographic structure of certain solids.[1] Water vortices are especially interesting because of their substantial relevance in a variety of technological and engineering contexts. These dynamic water motions are utilized in numerous applications, including hydraulic power generation,[2] water purification processes, such as hydrodynamic vortex separation,[3] water vortex-based air purification,[4] and river engineering.[5] The operational principles of these applications are complex, encompassing phenomena such as cavitation, gas diffusion, and the mechanical forces resulting from the high velocities present in the vortices.[6,7] In order to understand the mechanism of the complex turbulent structure of water vortices in various applications, it is necessary to develop computational models to describe the vortex behavior and its evolution. Such models have been published for a water vortex

30 September 2024 13:54:38

© Author(s) 2024

power plant,[8] vortex separator,[9] Taylor–Couette flow system,[10] and vortex formation in the cylindrical reactor.[11] Recently, there has been an increased focus on the aeration potential of water vortices,[12,13] especially when configured within hyperbolic geometries.[7] This line of research is considered a promising energy-efficient alternative to traditional aeration techniques, such as cascade systems or bubble diffusers.[14] Furthermore, in Ref. 15, the combination of a hyperbolic water vortex and plasma discharge has been shown to be an effective technology for the degradation of aqueous micro-pollutants, in particular due to the mixing and gas dissolution properties of the vortex.

Despite this interest, the fundamental processes that drive vortex-induced gas dissolution are not fully understood, particularly regarding the impact of specific reactor geometries on aeration efficiency. As was shown elsewhere,[7] a water vortex in hyperbolic funnels can form three regimes (Twisted, Straight, and Restricted). The formation of these regimes depends on the funnel geometry and the tangential velocity of the water flow. All three regimes have different parameters, such as the area of the water–air interface, hydraulic retention time (HRT), and oxygen dissolution rate. For all funnels tested, the Twisted and Straight regimes were found to be the most effective in terms of aeration. However, in order to elucidate the mechanisms of the hyperbolic water vortex operation and to optimize the design of vortex-based aeration systems, further research is needed. Computational fluid dynamics (CFD) simulations have been utilized to study air–water vortices in various contexts. These simulations have incorporated a range of dimensionless parameters and models to predict the behavior of air-core vortices at hydraulic intakes.[16] Additionally, the comparison between the Lagrangian and Eulerian approaches in vortex flow simulation has been investigated, revealing that both methods are capable of simulating the vortex flow, with the Lagrangian approach having greater computational cost but lower accuracy.[17] Overall, CFD simulations and experimental studies have contributed to a better understanding of air–water vortices and their characteristics.

Through a combined approach of experimental measurements and CFD modeling, the current work aims to deepen our understanding of the intricate interplay between vortex dynamics, reactor geometry, and aeration efficiency.[18] Such insight is crucial for the development of optimized aeration systems that harness the potential of water vortices, paving the way for enhanced energy efficiency and sustainability in various engineering applications, including wastewater treatment,[19,20] aquaculture,[21] and environmental remediation.[22]

II. EXPERIMENTAL SETUP AND NUMERICAL MODELING

The experimental setup (Fig. 1) comprises two sections: the funnel and the extension. The funnel consists of hyperbolic and cylindrical sections with a tangential water inlet and air vent on the top, while the extension includes the portion beneath the hyperbolic section with the bend and the outlet tubes. In the experiments [Fig. 1(b)], the flow exits through two outlet tubes to reduce back pressure and enhance the system's operating range.[23]

Based on the inlet mass flow rate of water and outlet pressure (located beneath the hyperbolic section), a number of distinct vortical structures can emerge in the hyperbolic section. A detailed discussion of the different experimental regimes can be found in Refs. 15 and 23.

The two vortex regimes with the highest experimental oxygen transfer rates, Twisted and Straight Schauberger (Fig. 2),[15,23] are obtained by varying the inlet flow rate of water. The flow rate values and the associated volume fractions of the water vortical structures in the funnel section are summarized in Table I.

A. Computational domain

Figure 3 illustrates the 3D CAD model used for CFD analysis and its sectional view with dimensions. In this study, the Twisted and Straight regimes are analyzed. To avoid using unstructured mesh in the computational domain, the water inlet tube is not explicitly modeled; instead, its intersection with the cylindrical part is defined as a boundary face [Fig. 3(a)]. A single outlet tube is employed in the computational domain, unlike two outlet tubes used in experiments (Fig. 1). This results in additional back pressure at the funnel exit, causing the interface to be smoother in the CFD simulations compared to the experimental observations (detailed explanation in Ref. 25).

B. Meshing

Structured meshes are known to provide better resolution of vortex flow field compared to unstructured meshes.[26] Therefore, a radially structured hexahedral mesh is generated using the meshing software Pointwise V18.4. Following the recommendations of Hernandez-Perez *et al.*[27] for turbulent two-phase pipe flows, a butterfly mesh structure is employed. This structure consists of a central cartesian mesh surrounded by a cylindrical mesh, as depicted in Figs. 4(a) and 4(b) (detailed mesh formation methodology is outlined elsewhere[25]).

In the present study, four different meshes are used for the mesh independence study, and their details are given in Table II. The results obtained on these meshes are discussed in Sec. III A.

C. Vorticity

Since aeration depends on the mixing of air and water, and this mixing can be qualitatively characterized by the *vorticity* in the system, a short explanation of vorticity is provided. The vorticity vector ($\boldsymbol{\Omega}$) represents how a fluid element would spin locally and is a vector quantity defined at every location in the flow field. It is defined as the curl of the velocity field and can be expressed as

$$\boldsymbol{\Omega} = \nabla \times \boldsymbol{u} = [\Omega_r, \Omega_\theta, \Omega_z] = \left[\frac{1}{r}\frac{\partial u_z}{\partial \theta} - \frac{\partial u_\theta}{\partial z}, \frac{\partial u_r}{\partial z} - \frac{\partial u_z}{\partial r}, \frac{1}{r}\frac{\partial r u_\theta}{\partial r} - \frac{1}{r}\frac{\partial u_r}{\partial \theta}\right], \quad (1)$$

where $\boldsymbol{u}$ is a velocity field [Fig. 4(c)], specified by the vector sum, given as

$$\boldsymbol{u} = u_r \hat{e}_r + u_z \hat{e}_z + u_\theta \hat{e}_\theta, \quad (2)$$

with u_r, u_z, u_θ the velocity components in radial, axial, and azimuthal/tangential directions and $\hat{e}_r, \hat{e}_z, \hat{e}_\theta$ the unit vectors along those directions, respectively.

Vorticity differs from the rotation of fluid; the former denotes local spinning of a fluid element, while the latter describes how a fluid element follows curved trajectories around an axis with certain angular velocity. Considering two velocity field distributions that have only a tangential component, namely $u_\theta \propto 1/r$ and $u_\theta \propto r$. In both these flows, the fluid rotates around an axis (following curved streamlines) with a certain angular velocity. For the first distribution with $u_\theta \propto 1/r$, the vorticity is zero and fluid elements do not spin locally. Such flows are known as irrotational flows. In the second case with $u_\theta \propto r$, the vorticity field is non-zero, and hence, such flows are

30 September 2024 13:54:38

© Author(s) 2024

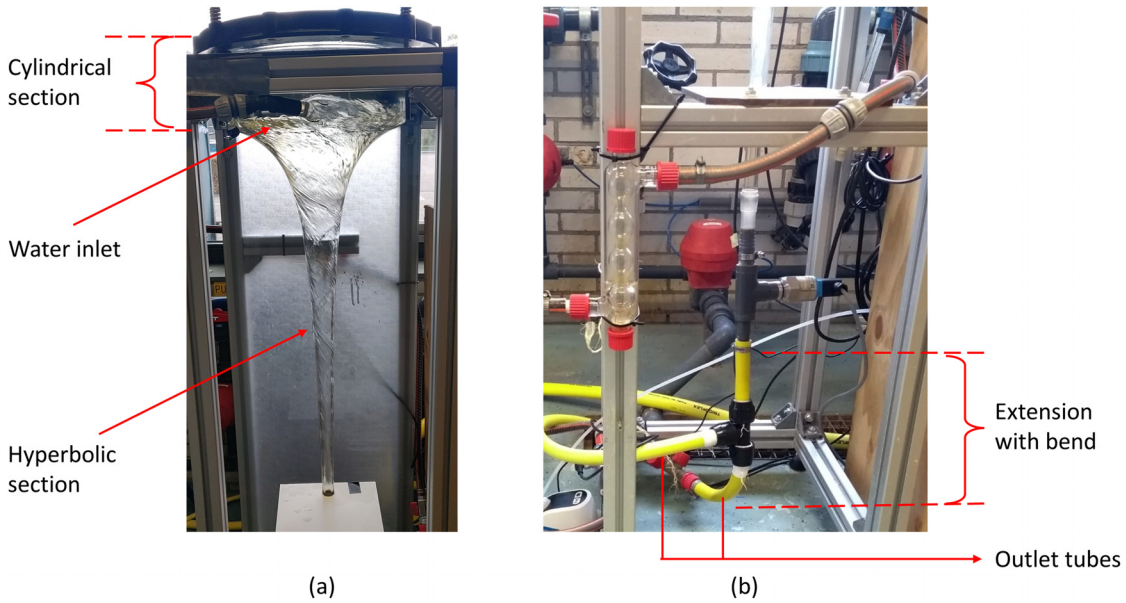

FIG. 1. Experimental setup divided into (a) funnel and (b) extension parts.

classified as rotational flows. This is also referred to as solid body rotation and it can be shown that in such a flow, the vorticity of a fluid element is equal to twice the angular velocity of the fluid.

D. Multiphase modeling

In both the Twisted and Straight regimes (Fig. 2), the phases are separated by a spatially varying interface and the relative motion between the phases is minimal in vortex flow systems.[26] To precisely track the evolution of this interface, the homogeneous volume of fluid (VOF) approach was utilized for multiphase modeling, based on previous literature studies.[26,28,29] In this approach, each computational cell is assigned a volume fraction ϕ_α defined as

$$\phi_\alpha = \frac{V_\alpha}{V}, \tag{3}$$

where V_α is the volume occupied by the phase α in a computational cell of volume V. The present system consists of two phases (gas and liquid represented by g and l), and the summation of their volume fraction in each computational cell is unity,

$$\phi_l + \phi_g = 1. \tag{4}$$

Each computational cell is assumed to be filled with one of the phases (liquid if $\phi_l = 1$ or gas if $\phi_l = 0$) or to be located in the interfacial region ($0 < \phi_l < 1$). In the homogeneous Euler–Euler-based VOF approach, it is assumed that the transported quantities, such as velocity and other turbulence fields, are shared by both phases. Hence, a single bulk momentum equation with variable density and viscosity is solved instead of solving the transport equations for each phase. This can be expressed as

$$\frac{\partial}{\partial t}(\rho u_j) + \frac{\partial}{\partial x_i}(\rho u_i u_j) = -\frac{\partial P}{\partial x_j} + \frac{\partial}{\partial x_i}(2\mu S_{ij}) + \rho g_j, \tag{5}$$

where the mixture quantities can be expressed as

$$\rho = \phi_l \rho_l + \phi_g \rho_g, \tag{6}$$

$$\mu = \phi_l \mu_l + \phi_g \mu_g. \tag{7}$$

The effects of surface tension were neglected in the present study based on the Weber number criteria.[30] The spatial and temporal

FIG. 2. Exemplary experimental images of the (a) Twisted and (b) Straight regimes.[15,23,24]

30 September 2024 13:54:38

© Author(s) 2024

TABLE I. Characterization of flow regimes.[7,24]

	Flow rate (L/min)		Water volume (%)		SAE (kg O_2/kWh)	
Flow regime	Min	Max	Min	Max	Min	Max
Twisted Schauberger	19.9	20.9	39	65	10.0	23.1
Straight Schauberger	22.0	23.0	91	95	5.5	5.5

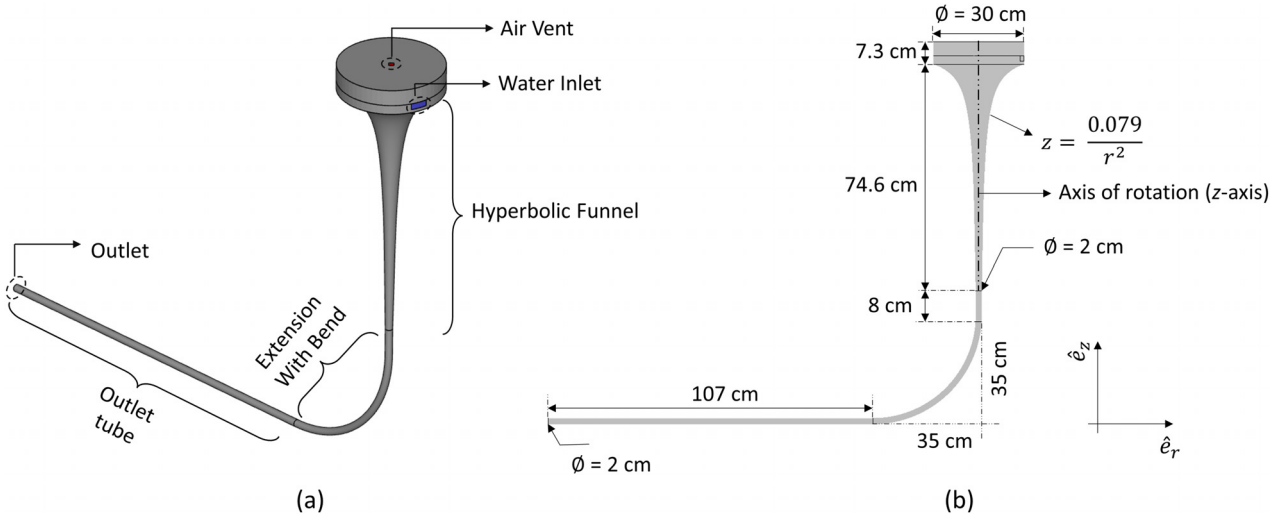

FIG. 3. Computational domain in (a) 3D and (d) sectional view with dimensions.

evolution of the interface was obtained from the solution of the continuity equation for the volume fraction given by

$$\frac{\partial \phi_k}{\partial t} + \frac{\partial}{\partial x_j}(\phi_k u_i) = 0. \tag{8}$$

This equation was solved for one of the phases, and the volume fraction of the other phase was obtained using Eq. (4). The VOF approach utilizes a geometric reconstruction method, employing a piecewise linear interface calculation (PLIC) to approximate the interface as a plane within the three-dimensional computational cell.[30]

E. Turbulence modeling

The unsteady turbulent flow is resolved across space and time using unsteady Reynolds averaged Navier–Stokes equation (URANS). In this approach, using Reynolds decomposition[31] the flow variables (velocity field u and pressure field p) are viewed as a

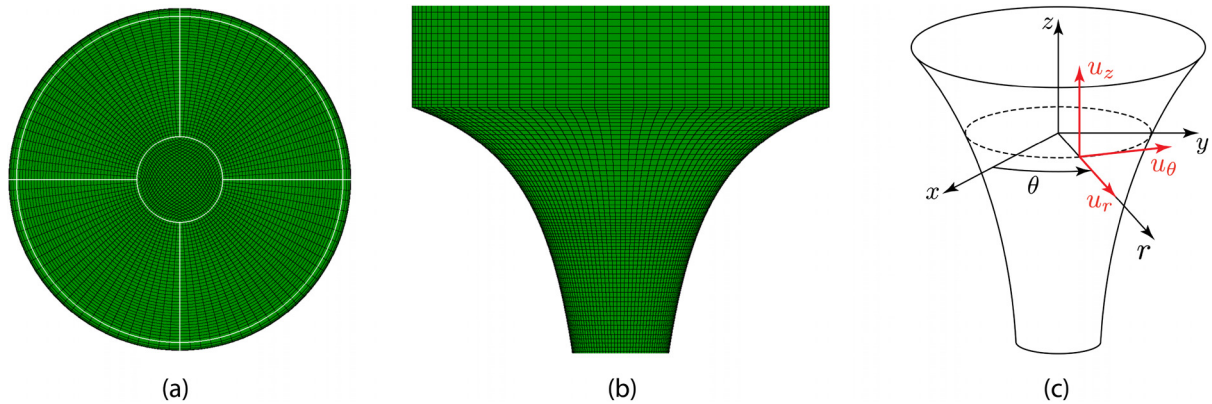

FIG. 4. 3D radially structured hexahedral butterfly mesh structure; (a) top-view of the cylindrical, (b) front view of hyperbolic funnel sections, and (c) cylindrical coordinate system.

30 September 2024 13:54:38

© Author(s) 2024

TABLE II. Meshes used for mesh independence study.

S. No.	Mesh	Node count	Cell count
1	500k	495 000	507 620
2	1mil	1 085 440	1 105 716
3	2mil	1 994 675	2 023 896
4	3mil	3 020 440	3 057 147

superimposition of their mean (U, P) and fluctuating values (u', p') given as

$$u = U + u', \tag{9}$$

$$p = P + p'. \tag{10}$$

Substituting these into Navier–Stokes equations in the general coordinate system[25] results in a set of equations referred to as the URANS equations,

$$\frac{\partial U_i}{\partial x_i} = 0, \tag{11}$$

$$\frac{\partial U_i}{\partial t} + U_j \frac{\partial U_i}{\partial x_j} = -\frac{1}{\rho}\frac{\partial P}{\partial x_i} + \frac{\partial}{\partial x_j}(2\nu s_{ij}) - \frac{\partial}{\partial x_j}\left(\overline{u_i' u_j'}\right), \tag{12}$$

where ν is the viscosity coefficient and s_{ij} is the strain rate tensor,

$$s_{ij} = \frac{1}{2}\left(\frac{\partial U_i}{\partial x_j} + \frac{\partial U_j}{\partial x_i}\right), \tag{13}$$

and $(\overline{u_j' u_i'})$ is the Reynolds stress tensor. The latter, requires additional closure modeling, which is achieved through the utilization of eddy viscosity models in this study. The shear stress transport (SST)-based $k - \omega$ model with curvature correction (CC) was employed in the present study based on the recommendations provided by Škerlavaj *et al.*[32] and Mulligan.[26] Detailed mathematical descriptions thereof can be found elsewhere.[30,33]

F. Boundary conditions and solver settings

The three boundary conditions for the present system (Fig. 3), namely, the water inlet, the air vent, and the outlet, were modeled as mass flow inlet, pressure outlet, and outflow boundary conditions, respectively. The associated variables are indicated in Table III, and a comprehensive review of the influence of different boundary conditions, along with the solution strategy, can be found elsewhere.[25]

A pressure-based solver is employed since both phases were nearly incompressible under the experimental conditions. The pressure–velocity coupling is achieved using a coupled scheme that enabled the use of larger time steps.[30] The PRESTO scheme is utilized for pressure interpolation at cell faces,[30] and second-order upwind schemes were applied for the advection in the momentum and other transport equations. An implicit volume formulation is employed to track the transient evolution of the vortex, based on the volume-of-flow continuity equation, with a compressive advective scheme for spatial discretization of the volume fraction. A bounded second-order implicit scheme is employed for the transient formulation to enhance numerical stability with larger time step sizes.

TABLE III. Boundary conditions.

Boundary	Type	Variables	Symbol
Water inlet	Mass flow inlet	Flow rate (water)	$\dot{m}_{water,in}$
		Tangential component	t
		Radial component	r
Air vent	Pressure outlet	Static gauge pressure	$P_{s,a}$
Outlet	Pressure outlet	Static gauge pressure	$P_{s,w}$
	Outflow	...	...

III. RESULTS AND DISCUSSION

A. Mesh independence study

For the mesh independence study, a specific input water flow of 21.5 L/min is chosen to induce a vortex structure on four different meshes ranging from 0.5×10^6 to 3×10^6 cells. The parameters of interest are measured in the funnel section, as its hydrodynamics are crucial for the present study. These parameters include the volume fraction of air (V_{air}), air–water interfacial area (A_{int}), and average exit pressure at the outlet ($P_{exit,\,avg}$). Table IV compares the steady-state values of these parameters for each mesh. The difference in values between the 1×10^6 and 2×10^6 cell meshes is less than 5% for all variables, which further decreases when transitioning to the 3×10^6 cell mesh. However, considering an increase in computation time by nearly 50% on the 3×10^6 cells (19 000 CPU hours) mesh compared to 2×10^6 cells (10 000 CPU hours), the 2×10^6 cell mesh is selected for simulations and analysis.

B. Validation

Simulations are performed for flow rates corresponding to Twisted ($\dot{m}_{water,in} = 20.9$ L/min) and Straight ($\dot{m}_{water,in} = 22.5$ L/min) regimes on the 2×10^6 mesh. The obtained vortical structures are shown in Figs. 5 and 6 along with the experimental images. Qualitatively, the CFD results reproduce the experimental vortical structures well, as seen in these figures by the air–water interface's shape and the air-core's volume formed. The wavy profile on the interface is also well captured in the CFD results. Additionally, the water volume fraction in the funnel section obtained from the CFD simulations is in good agreement with the experimental data, as indicated in Table V.

To further validate the numerical results, the radial position of the air–water interface along the axial distance of the funnel was compared with experimental data (the radial and axial distances are non-dimensionalized using cylindrical section diameter and height of the funnel section, respectively). The average interfacial position from

TABLE IV. Parameters of interest on different meshes.

Mesh	V_{air} (%)	A_{int} (cm^2)	$P_{exit,avg}$ (Pa)
500k	53.93	1551.83	1397.31
1mil	50.27	1470.67	1458.21
2mil	49.19	1415.08	1493.1
3mil	48.31	1384.8	1508.62

30 September 2024 13:54:38

© Author(s) 2024

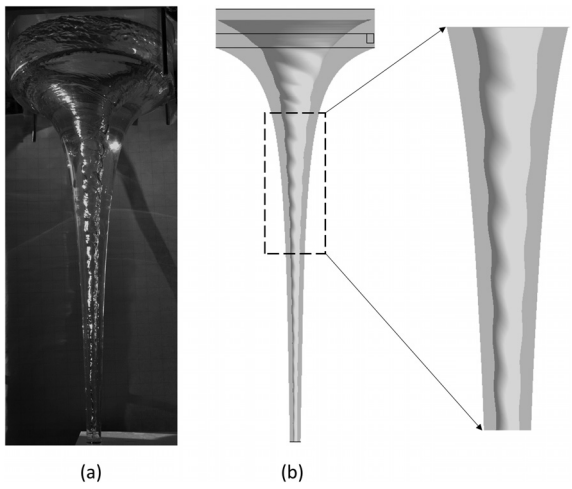

FIG. 5. Comparison of vortical structure for the Twisted regime ($\dot{m}_{water,in} = 20.9$ L/min); (a) experimental and (b) CFD.

experimental images at specific axial heights was manually extracted using open-source software.[34] Figure 7 depicts the comparison for both regimes. The selected turbulence model accurately captures the interface position. The air-core diameter varies along the axial direction, mirroring the shape of the hyperbolically shaped boundary. This shape is less prominent in the Straight regime due to the higher flow rate of water, resulting in higher water volume fractions in the funnel section. Significant differences in the interface position are noticeable in the bottom portion of the funnel. This disparity may be attributed to the use of a single outlet tube after the bend section, leading to higher back pressure, whereas two tubes were used in the experiments.

C. Flow organization

The time-averaged velocity distribution in the water phase was analyzed at three non-dimensional heights ($\xi = z/h$) from the exit of the funnel as depicted in Fig. 8. Here, ξ equal to 1 represents the height of the water inlet, while ξ equal to 0 represents the end of the funnel.

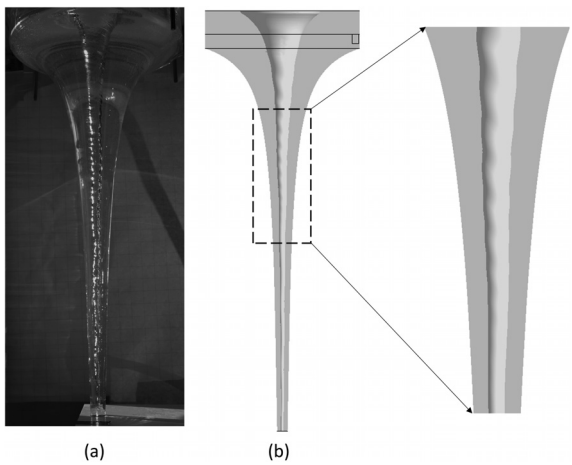

FIG. 6. Comparison of vortical structure for the Straight regime ($\dot{m}_{water,in} = 22.5$ L/min); (a) experimental and (b) CFD.

TABLE V. Water volume fraction (in %) in the funnel section.

	Experimental[24]	CFD
Twisted	49	51
Straight	94	90

1. Instabilities in the secondary flow field

The secondary flow field (radial and axial velocities) needs to be understood on a fundamental level to understand the high gas transfer rates in the system. Plotting the streamlines on a mid-sectional plane for both the regimes, as shown in Figs. 9 and 10, they show the presence of Taylor-like vortices. The streamlines are similar to the ones observed in other studies on strong vortices.[26,35] Hence, instabilities arise in both vortical structures' secondary flow fields.

The instabilities developed in the flow exhibit a 3D organization, with opposite spin directions of Taylor-like vortices evident in a section, as shown in Fig. 11 (water in blue). The simulation results (b) and (c) are compared here to results from a stereoscopic particle image velocimetry analysis (a) conducted by van de Griend.[36] Downward-traveling waves are observed on the interface, both experimentally and numerically. In Fig. 11, positions A and B represent approximate wavelengths of one such wave. Similar wave patterns were also observed in the work of Son *et al.*[35] These waves are attributed to the continuous axial translation of Taylor-like vortices due to incoming fluid into the system. The downward motion of Taylor-like vortices is evident from the velocity vectors at locations A and B. At the location of such a wave, the interface appears to bulge, and continuous

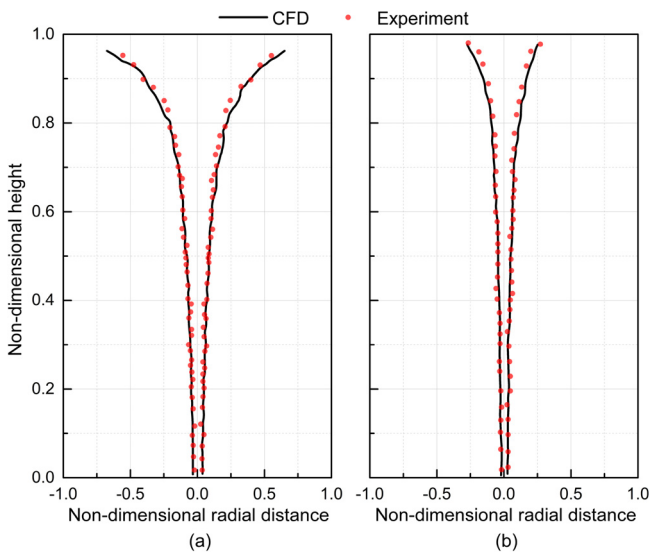

FIG. 7. Comparison of the air–water interface location between CFD and experiments for (a) twisted ($\dot{m}_{water,in} = 20.9$ L/min) and (b) straight ($\dot{m}_{water,in} = 22.5$ L/min) regimes.

30 September 2024 13:54:38

© Author(s) 2024

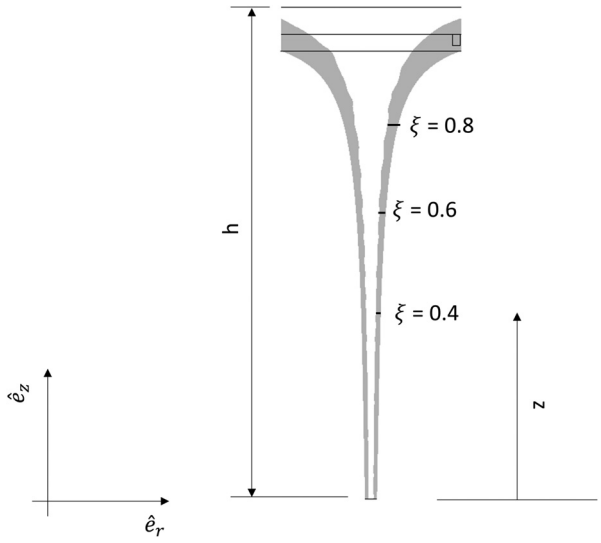

FIG. 8. Location of non-dimensional heights ξ.

generation of waves of varying wavelengths produces a 3D wavy profile on the interface.

D. Influence of hydrodynamics on gas transfer

To further investigate the rate of gas transfer, it is important to mention that it depends on

1 The average residence time of a fluid particle in the system, also known as hydraulic retention time (HRT).
2 Interfacial area (a_L).
3 Strength of mixing caused by secondary flow structures.
4 Concentration of species i in the interface and bulk liquid.

It is not possible to analyze parameter 4 with the current numerical model since mass transfer effects have not been included. However, the parameters mentioned in 1, 2, and 3 can be qualitatively analyzed using the obtained numerical results.

1. Hydraulic retention time (HRT)

The standard oxygen transfer rate (SOTR) is a metric used to quantify the amount of gas dissolved into the liquid phase. SOTR is inversely proportional to HRT and can be expressed as[7]

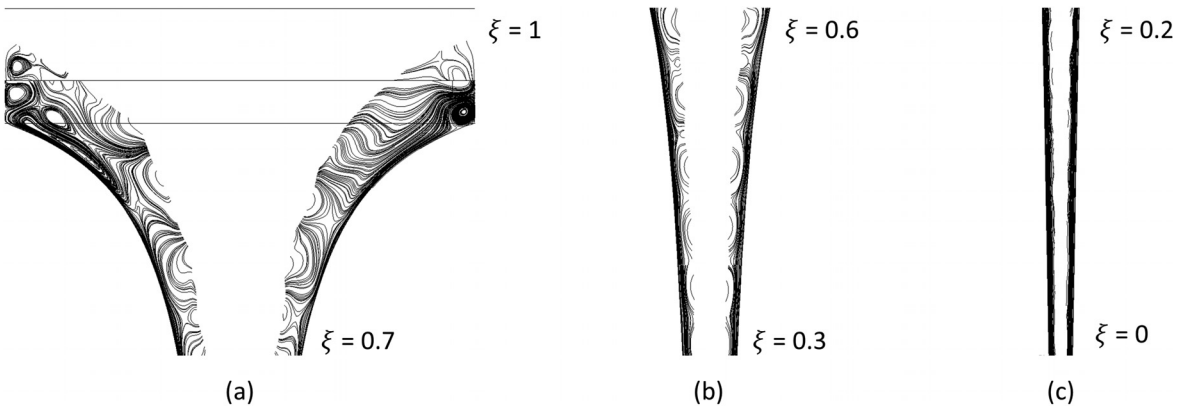

FIG. 9. Surface streamlines on the $r - z$ sectional plane for the Twisted regime ($\dot{m}_{water,in} = 20.9$ L/min).

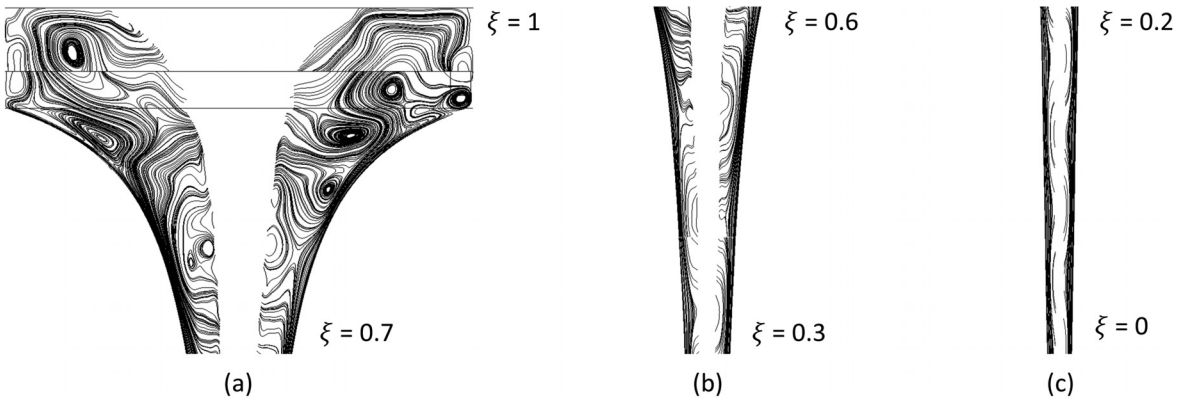

FIG. 10. Surface streamlines on a the $r - z$ sectional plane for the Straight regime ($\dot{m}_{water,in} = 22.5$ L/min).

30 September 2024 13:54:38

© Author(s) 2024

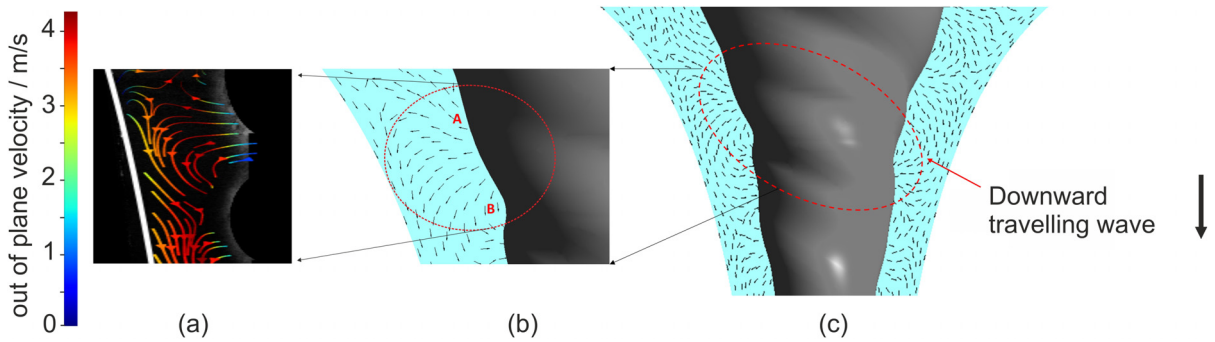

FIG. 11. Downward traveling wave. Results from stereoscopic particle image velocimetry in the (a) Twisted regime[36] compared to this simulation [(b) and (c)].

$$SOTR = \frac{VC_{20}}{1.024^{T-20}HRT}\ln\left(\frac{C_S - C_{in}}{C_S - C_{out}}\right), \tag{14}$$

where V is the water volume in the reactor, C_{20} is the dissolved oxygen (DO) at saturation for a temperature of 20 °C, T is the water temperature in °C, C_S is the DO concentration at saturation, C_{in} is the DO concentration in the feed, and C_{out} is the DO concentration in the bulk liquid.

Two competing forces are present in this system: circulatory and gravitational forces. The former tends to retain a fluid parcel for a longer time by inducing circular motion, thus increasing hydraulic retention time (HRT), while the latter decreases HRT by accelerating the fluid out of the funnel. From CFD simulation results, the transient path of water streamlines from the water inlet to the outlet was tracked. Each streamline differs in terms of the time (t_i) spent by it in the funnel section, depending on its path. A streamline traveling close to the walls of the funnel experiences less circulatory forces than gravitational forces, leading to very low HRTs. The opposite is true for a streamline traveling close to the air–water interface, a region of high tangential velocities with higher HRTs. Both of these scenarios are represented in Fig. 12, where the spheres on the streamline represent the position of an elemental fluid parcel at an interval of 0.5 s.

Figure 13 presents a plot of non-dimensional time ($\theta = t/t_i$) vs non-dimensional height (ξ) for streamlines originating from the water inlet and exiting at the end of the funnel, i.e., location I in Fig. 3. Through multiple regression analysis, it was observed that in the Twisted regime, a fluid parcel, on average, resides for 90% of its hydraulic retention time (HRT) within approximately half the height of the funnel (i.e., $\xi \geq 0.5$ for $\theta \leq 0.9$) and covers the remaining half in just around 10% of its HRT. In the Straight regime, we observe that a fluid parcel covers only 30% of the depth (i.e., $\xi \geq 0.7$ for $\theta \leq 0.9$) in 90% of its HRT due to higher circulatory forces.

Hence, the system can be divided into two sections with respect to HRT: Sec. I, in which fluid resides for most of its duration ($\theta \leq 0.9$) in the funnel, and Sec. II ($0.9 < \theta \leq 1$), which is predominantly the region with the least radius where the fluid rapidly accelerates and exits the funnel. The average HRTs in Twisted and Straight regimes from experiments are 18 and 29 s, respectively.[7] Purely based on the relation between water volume in the reactor and HRT, the Straight regime should exhibit higher aeration capabilities in comparison to the Twisted regime, but the experimental data indicate the opposite trend.[7] Hence, the other two parameters, i.e., interfacial area and mixing in the bulk of fluid, must be analyzed to reason this behavior. These parameters are analyzed in each of these sections of the funnel where Sec. I is the upper 40% height (i.e., $\xi \geq 0.6$ average of Twisted and Straight regimes) while Sec. II is the remaining portion ($0 \leq \xi < 0.6$).

2. Interfacial area

The air–water region directly affects the area available for the diffusion of gas molecules. Also, considering both phases are incompressible at the operating conditions in a fixed volume of funnel, more interfacial area implies that less mass of water (m_w) is present in the system. The 3D iso-surface of the interface in Sec. I for both regimes is shown in Fig. 14.

In Sec. I, the Twisted regime shows more than twice the interfacial area in comparison to the Straight regime as tabulated in Table VI. Also, in this section the Twisted regime contains 44% less mass of water [standard oxygen transfer rate (SOTR) varies inversely with the mass of water[7]]. In Sec. II, both the regimes contain a comparable mass of water (13% less in the Twisted regime). The added advantages

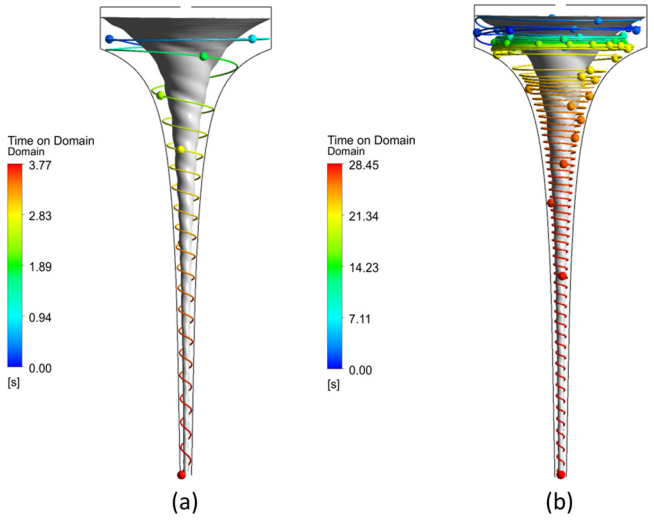

FIG. 12. Streamline paths near the (a) wall and (b) air–water interface region in the Twisted regime with 3D air-core iso-surface in gray and funnel wall boundaries in black.

30 September 2024 13:54:38

© Author(s) 2024

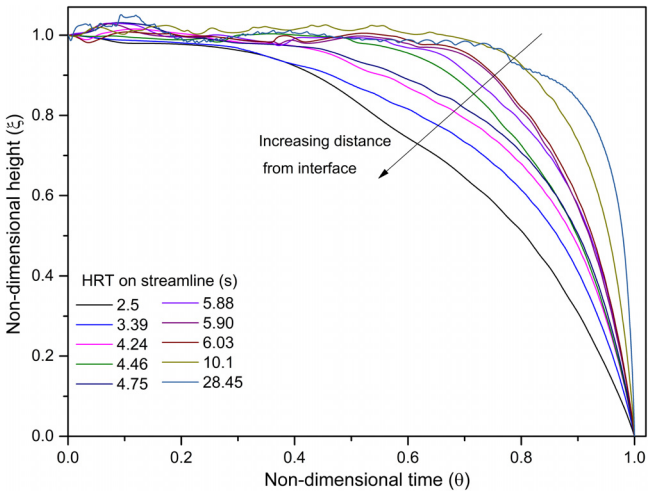

FIG. 13. Non-dimensional time vs height for streamlines in funnel section for the Twisted regime.

of the higher interfacial area and lower mass of water (m_w) facilitate higher SOTRs for the Twisted regime.

3. Mixing

Mixing can be qualitatively characterized by vorticity (Sec. II C). As a preliminary analysis, vorticity is analyzed in the r–z sectional plane as indicated in Fig. 8. The computed vorticity is normal to this plane, i.e., Ω_θ in Eq. (1). Wide scales of vorticity were observed in the domain. For instance, in the Twisted regime at the end of Sec. I ($\xi = 0.6$), Ω_θ varies from around 3300 s^{-1} at the wall to around 20 s^{-1} at the interface. The high values near the walls were due to no-slip boundary condition, but this does not contribute to mixing in the bulk. The plots of time-averaged vorticity along with velocity vectors projected onto this plane in both the regimes are shown in Figs. 15 and 16. In these figures, the scales of vorticity are chosen such that they are distinctly visible, excluding high vorticity values in the near-wall region.

The vorticity is higher near the interface due to the difference in velocity of phases at this location. With increasing depth, the magnitude of vorticity also increases, and this can again be attributed to the

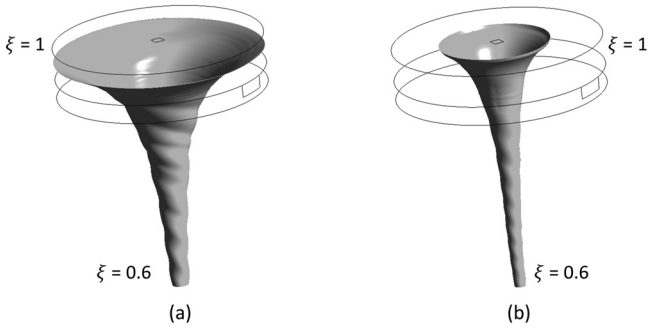

FIG. 14. Air–water interface in Sec. I in (a) Twisted and (b) Straight regimes.

TABLE VI. Comparison of regimes in terms of parameters governed by air–water interface.

Parameter	Regimes	Section I	Section II	Total
A_{int} (m^2)	Twisted	0.1213	0.0203	0.1416
	Straight	0.0568	0.0139	0.0708
	Ratio	2.1	1.5	2.0
V_{air} (%)	Twisted	50.2	23.6	49.2
	Straight	10.1	11.0	10.2
	Ratio	5.0	2.2	4.8
m_w (kg)	Twisted	4.2	0.26	4.4
	Straight	7.5	0.3	7.8
	Ratio	0.55	0.87	0.56

increase in axial velocities in the regions. The magnitude of volume average vorticity ($|\boldsymbol{\Omega}|$) is 40.6% higher in the Twisted regime (74.54 s^{-1}) in comparison to the Straight regime (53.03 s^{-1}). Hence, the Twisted regime benefits from higher interfacial areas, less mass of fluid, and higher vorticities than the Straight regime leading to the higher gas transfer rates experimentally observed.

IV. SUMMARY AND CONCLUSIONS

This study uses CFD simulations to model vortices within hyperbolic funnels and analyses their flow field organization, with the aim of understanding the underlying physical mechanisms responsible for the measured high gas transfer rates. The investigation yielded several key findings: First, a mesh independence study was conducted using ANSYS-Fluent 19R3 with varying mesh resolutions to analyze a specific water flow rate (Twisted regime) and induce a vortex structure. Increasing mesh resolution improved the resolution of the air–water interface. Parameters such as air-fraction, air–water interfacial area, and average exit static pressure were evaluated across different meshes. The 2 mil mesh was selected for further analysis due to computational efficiency. The SST-based k–ω turbulence model effectively captured interface locations for both the Twisted and Straight vortex regimes.

In particular, instabilities resembling counter-rotating Taylor-like vortices were observed in the secondary flow fields of both regimes. Drawing upon experimental findings and model calculations, a comparative analysis of the two regimes was carried out in terms of parameters influencing the gas dissolution rate relation between water volume in the reactor and HRT, air–water interface area, and bulk mixing. Despite the lower HRT, the Twisted regime exhibits significantly higher aeration efficiency due to the higher interfacial area and mean vorticity per unit water mass compared to the Straight regime, resulting in superior gas transfer rates.

The agreement between model and experiment is particularly evident in accurately capturing interface shapes and air-core volumes. Furthermore, the interface positions from simulations closely align with experimental data, validating the numerical approach employed. Flow organization was analyzed by studying velocity fields at various heights from the funnel exit. With increasing depth, tangential velocities increase due to the conservation of angular momentum. Axial velocities are mainly restricted to the walls and interface, influenced by circulatory and gravitational forces. Radial velocities are significant near the interface, contributing to vortex sustenance.

30 September 2024 13:54:38

© Author(s) 2024

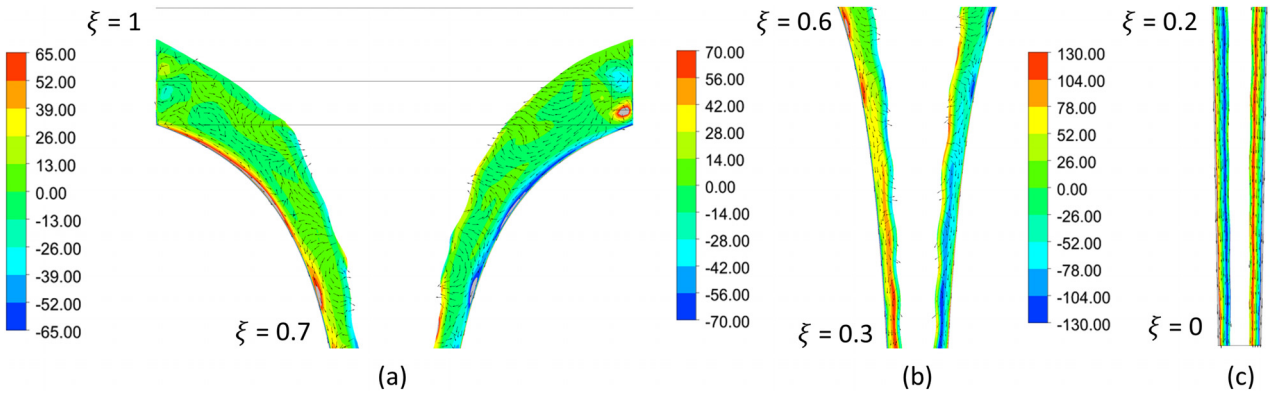

FIG. 15. Vorticity (Ω_θ) in $r - z$ sectional plane for the Twisted regime.

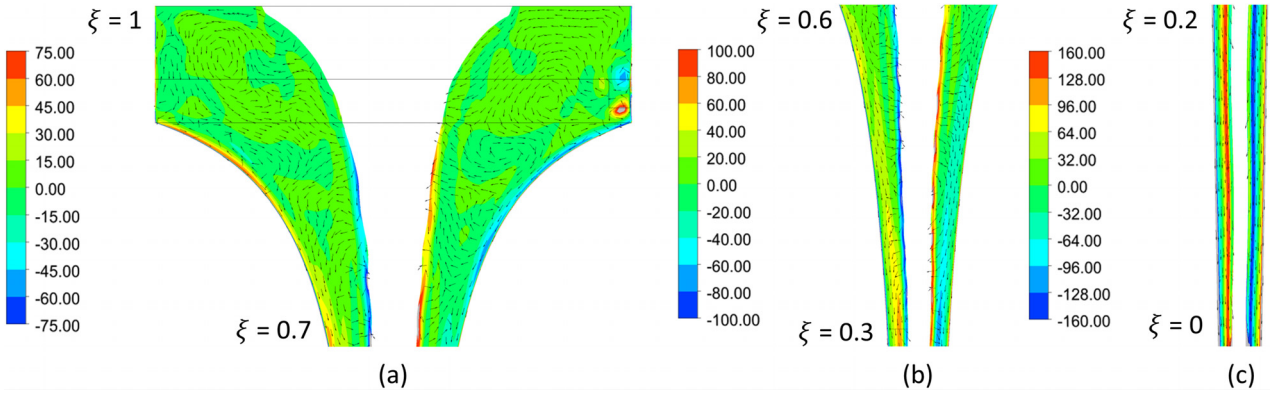

FIG. 16. Vorticity (Ω_θ) in $r - z$ sectional plane for the Straight regime.

Instabilities in the secondary flow field, such as Taylor-like vortices and interface waves, were also observed. Furthermore, the relation between water volume in the reactor and HRT, interfacial area, and vorticity are investigated to find dependencies on the gas dissolution rate of vortices in hyperbolic funnel. Analysis of HRT shows that fluid parcels near the interface had longer residence times. The Twisted regime has a lower HRT and water volume in the reactor compared to the Straight regime, but exhibits higher interfacial area and vorticity, resulting in increased gas transfer efficiency. A differential mass balance equation is proposed to explain gas transfer dynamics, taking into account variations in interfacial area, advection, and diffusion.

We have shown that CFD simulations performed using ANSYS-Fluent 19R3, with a mesh independence study showing improved resolution with increasing mesh density, can qualitatively represent and explain experimentally observed findings on the shape and the aeration capabilities of hyperbolic water vortices. This study demonstrated the utility of CFD simulations in elucidating the hydrodynamics of hyperbolic funnel systems and their impact on gas transfer processes. These findings underscored the significance of vortex organization in enhancing gas transfer efficiency, with implications for optimizing aeration mechanisms in various applications.

ACKNOWLEDGMENTS

This work was performed in the cooperation framework of Wetsus European Center of Excellence for Sustainable Water Technology (www.wetsus.eu) within the Applied Water Physics theme. Wetsus is cofounded by the Dutch Ministry of Economic Affairs and Ministry of Infrastructure and Environment, The Province of Fryslan, and the Northern Netherlands Provinces. The authors partially generated this text in part with GPT-3, OpenAI's large-scale language-generation model, as well as deepL neural machine translation for grammar and phrasing corrections. Upon generating the draft language, the authors reviewed, edited, and revised the language to their own liking and take ultimate responsibility for the content of this publication.

AUTHOR DECLARATIONS

Conflict of Interest

The authors have no conflicts to disclose.

Author Contributions

Teja Donepudi: Conceptualization (equal); Data curation (equal); Formal analysis (equal); Investigation (equal); Software (equal);

30 September 2024 13:54:38

© Author(s) 2024

Visualization (equal); Writing – original draft (equal); Writing – review & editing (equal). **Maarten van de Griend:** Conceptualization (equal); Investigation (equal); Supervision (equal); Validation (equal); Writing – review & editing (supporting). **Luewton L. F. Agostinho:** Conceptualization (equal); Project administration (equal); Supervision (equal); Writing – review & editing (equal). **Esther J. de Kroon:** Data curation (equal); Investigation (equal); Validation (equal). **Roman Klymenko:** Formal analysis (equal); Validation (equal); Writing – original draft (supporting); Writing – review & editing (equal). **Rene Pecnik:** Formal analysis (equal); Investigation (equal); Project administration (equal); Resources (equal); Software (equal); Supervision (lead); Validation (equal); Writing – review & editing (equal). **Jakob Woisetschlaeger:** Conceptualization (equal); Formal analysis (equal); Supervision (supporting); Visualization (supporting); Writing – review & editing (equal). **Elmar C. Fuchs:** Conceptualization (equal); Project administration (equal); Writing – original draft (equal); Writing – review & editing (equal).

DATA AVAILABILITY

The data that support the findings of this study are available from the corresponding author upon reasonable request.

REFERENCES

[1]J. H. E. Cartwright, A. G. Checa, B. Escribano, and C. Ignacio Sainz-Díaz, "Crystal growth as an excitable medium," Philos. Trans. R. Soc., A **370**, 2866 (2012).
[2]A. B. Timilsina, S. Mulligan, and T. R. Bajracharya, "Water vortex hydropower technology: A state-of-the-art review of developmental trends," Clean Technol. Environ. Policy **20**, 1737–1760 (2018).
[3]R. Y. G. Andoh, S. P. Hides, and A. J. Saul, "Improving water quality using hydrodynamic vortex separators and screening systems," in 9th International Conference on Urban Drainage (2002).
[4]S. U. Leea, J. Y. Leea, S. H. Leea, and G. W. Jeonb, "A sustainable water vortex-based air purification for indoor air quality," Build. Environ. **243**, 110610 (2023).
[5]F. Fitzke, Instream River Training (IRT) (2023).
[6]Y. Motoori and S. Goto, "Generation mechanism of a hierarchy of vortices in a turbulent boundary layer," J. Fluid Mech. **865**, 1085–1109 (2019).
[7]R. Klymenko, H. Nanninga, E. de Kroon, L. L. F. Agostinho, E. C. Fuchs, J. Woisetschläger, and W. F. L. M. Hoeben, "Preparation of free-surface hyperbolic water vortices," JoVE **197**, e64516 (2023).
[8]D. Powalla, S. Hoerner, O. Cleynen, N. Müller, J. Stamm, and D. Théven, "A computational fluid dynamics model for a water vortex power plant as platform for etho-and ecohydraulic research," Energies **14**, 639 (2021).
[9]S. Mulligan, D. McDermott, and E. Clifford, "Multiphase numerical modelling of hydraulic structures with rapidly rotating flows: Stormwater vortex hydrodynamic separator," in 7th International Symposium on Hydraulic Structures (2018).
[10]S. Mulligan, G. D. Cesare, J. Casserly, and R. Sherlock, "Understanding turbulent freesurface vortex flows using a Taylor-Couette flow analogy," Sci. Rep. **8**, 824 (2018).
[11]T. C. Kueh, S. L. Beh, D. Rilling, and Y. Ooi, "Numerical analysis of water vortex formation for the water vortex power plant," Int. J. Innovation, Manage. Technol. **5**, 111–115 (2014).
[12]M. V. van de Griend, F. Warrener, M. van den Akker, Y. Song, E. C. Fuchs, W. Loiskandl, and L. L. F. Agostinho, "Vortex impeller-based aeration of groundwater," Water **14**, 795 (2022).
[13]P. Wójtowicz and M. Szlachta, "How effective is aeration with vortex flow regulators? pilot scale experiments," E3S Web Conf. **22**, 00190 (2017).
[14]H. J. Popel, *Aeration and Gas Transfer* (Delft University of Technology, 1976).
[15]R. Klymenko, E. de Kroon, L. L. F. Agostinho, E. C. Fuchs, J. Woisetschläger, and W. F. L. M. Hoeben, "Characterization of a hyperbolic vortex plasma reactor for the removal of aqueous phase micropollutants," J. Phys. D: Appl. Phys. **57**, 215204 (2024).
[16]J. E. Hite and W. C. Mih, "Velocity of air-core vortices at hydraulic intakes," J. Hydraul. Eng. **120**, 284 (1994).
[17]M. Azarpira, A. R. Zarrati, and P. Farrokhzad, "Comparison between the Lagrangian and Eulerian approach in simulation of free surface air-core vortices," Water **13**, 726 (2021).
[18]Y. G. Erika Pittoors and S. W. H. V. Hulle, "Modeling dissolved oxygen concentration for optimizing aeration systems and reducing oxygen consumption in activated sludge processes: A review," Chem. Eng. Commun. **201**, 983 (2014).
[19]H. He, B. M. Wagner, A. L. Carlson, C. Yang, and G. T. Daigger, "Recent progress using membrane aerated biofilm reactors for wastewater treatment," Water Sci. Technol. **84**, 2131 (2021).
[20]B. Ji, "Towards environment-sustainable wastewater treatment and reclamation by the non-aerated microalgal-bacterial granular sludge process: Recent advances and future directions," Sci. Total Environ. **806**, 150707 (2022).
[21]M. Mohan, B. P. Ch, G. S. Prasad, R. Srinu, A. Konduri, D. P. M. K. Goud, and M. K. Kumar, "Application and importance of aeration system in aquaculture pond: A review," Asian J. Microbiol. Biotechnol. Environ. Sci. **24**, 370–376 (2022).
[22]X. Li, D. Bao, Y. Zhang, W. Xu, C. Zhang, H. Yang, Q. Ru, Y-f Wang, H. Ma, E. Zhu, L. Dong, L. Li, X. Li, X. Qiu, J. Tian, and X. Zheng, "Development and application of membrane aerated biofilm reactor (MABR)—A review," Water **15**, 436 (2023).
[23]L. L. Agostinho, R. Pecnik, J. Woisetschläger, E. de Kroon, N. Şişcanu, M. V. van de Griend, W. Loiskandl, and E. C. Fuchs, "Enhanced oxygen volumetric mass transfer in a geometrically constrained vortex," Water **14**, 771 (2022).
[24]E. de Kroon, "Iron oxidation in groundwater using a hyperbolic water vortex system," M.S. thesis (Van Hall Larenstein University of Applied Sciences, 2021).
[25]T. Donepudi, "Vortices in hyperbolic funnels as aeration systems: A numerical study," M.S. thesis (Delft University of Technology, Netherlands, 2021).
[26]S. Mulligan, "Experimental and numerical analysis of three-dimensional free-surface turbulent vortex flows with strong circulation," Ph.D. thesis (Institute of Technology Sligo, Ireland, 2015).
[27]V. Hernandez-Perez, M. Abdulkadir, and B. Ay 9zzopardi, "Grid generation issues in the CFD modelling of two-phase flow in a pipe," J. Comput. Multiphase Flows **3**, 13 (2011).
[28]F. Suerich-Gulick, S. Gaskin, M. Villeneuve, G. Holder, and E. Parkinson, "Experimental and numerical analysis of free surface vortices at a hydropower intake," in Proceedings of the 7th International Conference on HydroScience and Engineering (2006); available at https://researchdiscovery.drexel.edu/esploro/outputs/journalArticle/Experimental-and-numerical-analysis-of-free/991014632938404721/filesAndLinks ?index=0.
[29]H. Shabara, O. Yaakob, Y. M. Ahmed, and A. Elbatran, "CFD simulation of water gravitation vortex pool flow for mini hydropower plants," J. Teknol. **74**, 77–81 (2015).
[30]*ANSYS FLUENT 12.0 Theory Guide* (ANSYS, Inc., 2009).
[31]P. W. Egolf and K. Hutter, *Nonlinear, Nonlocal and Fractional Turbulence* (Springer, 2020), pp. 13–18.
[32]A. Škerlavaj, L. Škerget, J. Ravnik, and A. Lipej, "Predicting free-surface vortices with single-phase simulations," Eng. Appl. Comput. Fluid Mech. **8**, 193 (2014).
[33]S. B. Pope, *Turbulent Flows* (Cambridge University Press, 2000).
[34]See https://automeris.io/WebPlotDigitizer/ for "Webplotdigitizer.".
[35]J. H. Son, C. H. Sohn, and I. S. Park, "Numerical study of 3-D air core phenomenon during liquid draining," J. Mech. Sci. Technol. **29**, 4247 (2015).
[36]M. van de Griend, "On the theory and applications of hyperbolic water vortices," Ph.D. thesis (University of Natural Resources and Life Sciences, Vienna, 2023).

30 September 2024 13:54:38

© Author(s) 2024